ADVANCED ENERGY MATERIALS
www.advenergymat.de

3D Printed SnSe Thermoelectric Generators with High Figure of Merit

Matthew R. Burton, Shahin Mehraban, David Beynon, James McGettrick, Trystan Watson, Nicholas P. Lavery, and Matthew J. Carnie**

Since the discovery of the record figure of merit (ZT) of 2.6 ± 0.3 in tin selenide (SnSe), the material has attracted much attention in the field of thermoelectrics. This paper reports a novel pseudo-3D printing technique to fabricate bulk SnSe thermoelectric elements, allowing for the fabrication of standard configuration thermoelectric generators. In contrast to fabrication examples presented to date, this technique is potentially very low-cost and allows for facile, scalable, and rapid fabrication. Bulk SnSe thermoelectric elements are produced and characterized over a wide range of temperatures. An element printed from an ink with 4% organic binder produces the highest performance, with a ZT value of 1.7 (±0.25) at 758 K. This is the highest ZT reported of any printed thermoelectric material, and the first bulk printed material to operate at this temperature. Finally, a proof-of-concept, all printed SnSe thermoelectric generator is presented, producing 20 µW at 772 K.

1. Introduction

In the field of thermoelectric materials, the figure of merit (ZT) is used to compare the ability of materials to harvest heat energy (Equation (1)). The more efficient a material is at converting heat into electrical power, the higher a ZT value that material has. The figure of merit equation is composed of the transport characteristics of: S the Seebeck coefficient (V K^{-1}), σ the electrical conductivity (S m^{-1}) and κ the thermal conductivity (W m^{-1} K^{-1}), along with T the temperature of the material (K).[1] The material properties are, however, interrelated which results in the optimization of one property having simultaneous effects on the others.[2] This has led to a ZT of 1 being viewed as a significant value which can have efficiencies comparable to several other renewable technologies.[3]

$$\mathrm{ZT} = \frac{S^2\sigma}{\kappa}T \tag{1}$$

Thermoelectric research has been primarily focused on the chalcogen compounds of Bi_2Te_3 and PbTe for low and medium temperature applications respectively. The low earth abundance of Te (1 µg kg^{-1})[4] has limited the commercial viability of thermoelectric generators to niche applications, such as space[5] and watches[6] or use in reverse as Peltier coolers.[7] Several other groups of thermoelectric materials have been studied, such as oxides,[8] silicides,[9] and half heuslers.[10] Whilst the components of these materials are more Earth abundant than Te, ZT in these materials are lower than their Te counterparts, preventing the wider use of thermoelectric generators. In 2014, SnSe was shown to have a ZT of 2.6 in single crystal ingots along a preferential crystallographic plane denoted as the *b*-axis.[11] As a result this Te free compound has sparked much interest in the thermoelectric community. SnSe is also a material of much interest in the fields of photovoltaics (PV),[12] Li-ion and Na-ion batteries,[13] and supercapacitors.[14]

Many fabrication techniques for SnSe including solvothermal synthesis[15–17] or melting (M),[18–21] followed by spark plasma sintering (SPS) have been shown in the literature[15–22] along with cold pressing,[23] hot pressing,[24,25] and thermal evaporation,[26,27] since the discovery of the high figure of merit by Zhao et al.[11] Many of these techniques require high temperature, high pressure, and lengthy fabrication times. In contrast, printing can be achieved at room temperature, atmospheric pressure and can yield fast fabrication times in a scalable process. This technique has been studied for Bi_2Te_3.[28–30] Printing, with the notable exception of Kim et al.[30] who printed bulk Bi_2Te_3 samples with a ZT of up to 0.9 at 398 K, has only allowed for the fabrication of films in the order of 300 µm thick. These films are not advantageous

Dr. M. R. Burton, Dr. D. Beynon, Dr. J. McGettrick, Prof. T. Watson, Dr. M. J. Carnie
SPECIFIC
Materials Research Centre
College of Engineering
Swansea University
Bay Campus, Swansea SA1 8EN, UK
E-mail: m.r.burton@swansea.ac.uk; m.j.carnie@swansea.ac.uk
Dr. S. Mehraban, Dr. N. P. Lavery
MACH1
Materials Research Centre
College of Engineering
Swansea University
Bay Campus, Swansea SA1 8EN, UK
The ORCID identification number(s) for the author(s) of this article can be found under https://doi.org/10.1002/aenm.201900201.

DOI: 10.1002/aenm.201900201

to the manufacturing of bulk thermoelectric generators legs of a traditional configuration, where leg sizes are in the order of 1 mm × 1 mm × 2 mm. Medium and high temperature printed thermoelectric materials have not been explored to the same extent as Bi_2Te_3 with a notable exception reported by Han et al.,[31] where screen printed PbTe films exhibiting a ZT up to 1.02 at 669 K were reported on films of 20–30 µm in thickness. There are currently no reports of non-Bi_2Te_3 bulk printed samples being fabricated. The reports referenced here all use the low Earth abundant element Te and until now reports of SnSe have focused on single crystal ingots,[11,32] polycrystalline materials,[12–22] and thin films.[26,27,33]

2. Results and Discussion

2.1. Chemical and Structural Characterizations

The production of the SnSe ink is shown schematically in **Figure 1**a–f. The initial ball milling of Sn and Se, represented in

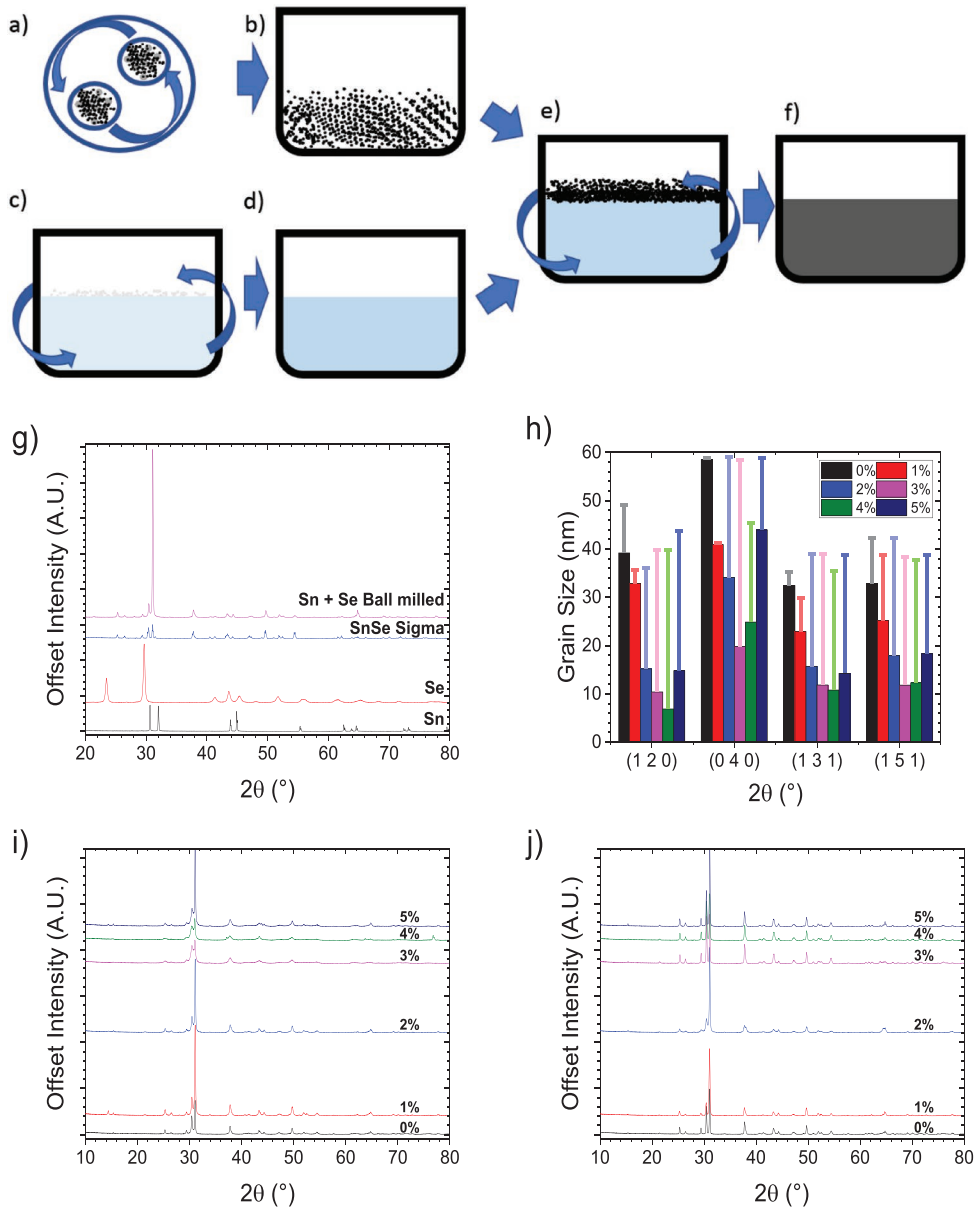

Figure 1. SnSe ink and device manufacturing technique: a) Sn and Se is loaded into a ball mill with stainless steel balls and set to spin, b) the resulting homogeneous powder, c) sodium carboxymethyl cellulose and deionized water are mixed together in a centrifugal mixer, d) a homogeneous liquid is produced, e) the powder from (b) and the liquid from (d) are mixed together in a centrifugal mixer, and f) a homogeneous liquid is produced. X-ray diffraction: g) comparison of ball milled powder to commercial SnSe powder and starting materials, h) comparison of grain sizes from four peaks, before (columns) and after cure (bars) with all binder concentrations, i) diffraction patterns of tape cast films before cure, and j) diffraction patterns of tape cast films postcure.

Figure 1a, produced a powder. To confirm the powder produced was SnSe, X-ray diffraction (XRD) was conducted. Figure 1g reveals that the ball milled Sn and Se powder exhibits the same XRD peaks as the commercially available SnSe powder (Sigma-Aldrich), whilst lacking peaks from the initial Sn and Se powders. From this it was concluded that the ball milling process was sufficient to form a pure SnSe powder. To test the ink produced (as detailed in the Experimental Section) was conducive to printing SnSe, films ≈200 µm thick were tape cast onto glass. Diffraction patterns for the printed films are shown in Figure 1i,j before and after curing respectively, which reveal that no crystallographic change is observed from the printed process on the SnSe powder. This importantly shows that SnSe can be printed in this manner, knowledge of which is of interest the fields of thermoelectrics, PV, Li-ion and Na-ion batteries, and supercapacitors.

Comparing Figure 1i with Figure 1j reveals that after curing the films in He at 873 K, the diffraction peaks become more intense and narrower, indicating an enlargement of the crystallite size in the films (superimposed diffraction patterns are represented in Figure S1, Supporting Information). Using the Scherrer equation and assuming spherical particles, Figure 1h shows the crystallite size on four different diffraction peaks compared both pre- and postcure for all binder concentrations used. This would suggest that precure a higher concentration of binder restricts the crystallite size, postcure crystallite sizes are seen to be similar irrespective of percentage of binder used. This indicates that whilst the ink is drying at 120 °C in air, the SnSe powder undergoes a sintering step which can be limited with increased binder percentages. This interestingly allows for crystallite size control at low temperatures. Control of grain size is important for solar cell applications as all PV parameters can be affected by grain size,[34] and in thermoelectric applications too as crystallite size is known to affect the figure of merit.[35]

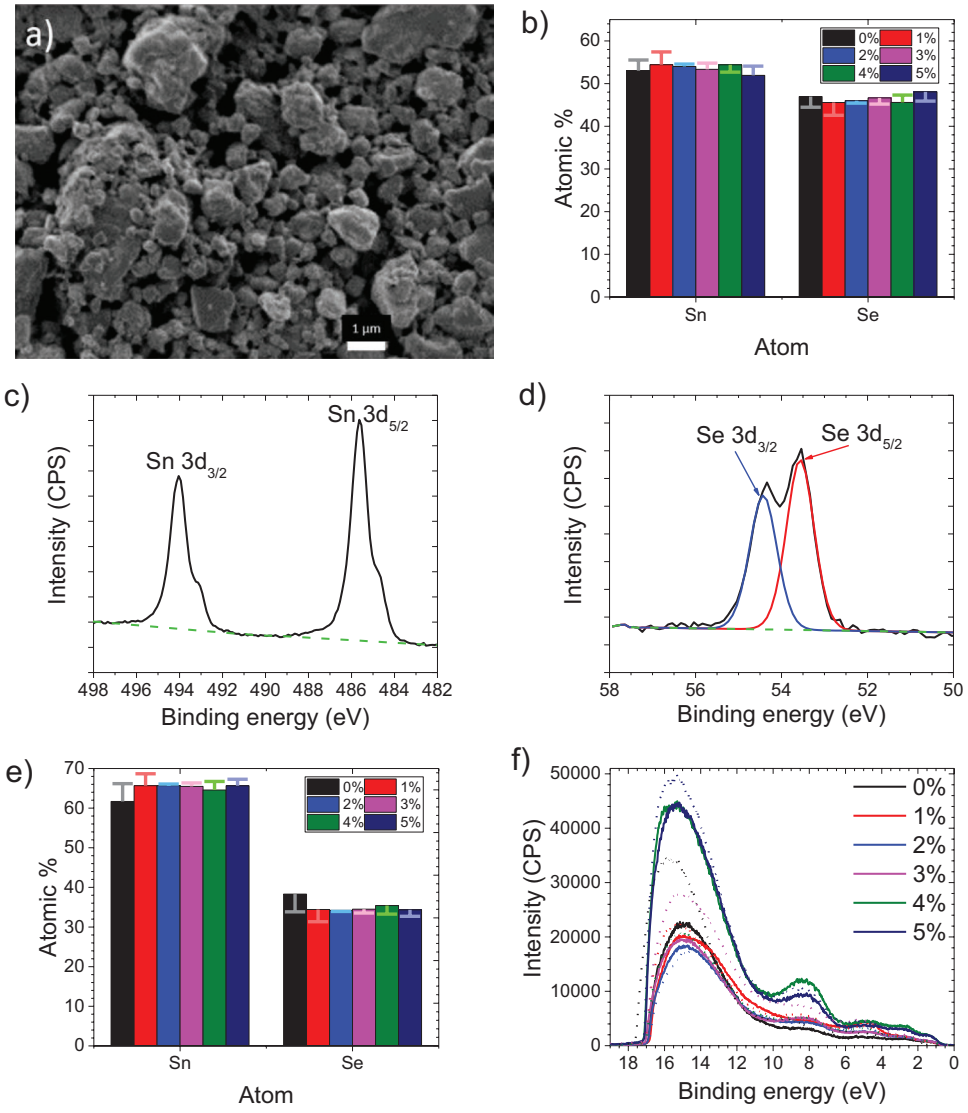

Figure 2. a) SEM image of 4% cured SnSe, b) EDX composition of samples before (columns) and after curing (bars), c) Sn XPS on 3% cured SnSe, d) Se XPS on 3% cured SnSe, e) XPS composition of samples before (columns) and after curing (bars), and f) UPS of samples before (dotted) and after (solid) cure.

Scanning electron microscopy (SEM) images of the tape cast films both precure and postcure (873 K in He) are shown in Figure S2 in the Supporting Information, whilst a typical example is shown in **Figure 2**a. No difference is observed between binder concentrations and between pre- and postcuring. The films are all seen to be porous with what appears to be randomly orientated particles. The composition of the films precure and postcure was studied by energy-dispersive X-ray spectroscopy (EDX) and X-ray photoelectron spectroscopy (XPS), with the resulting compositions shown in Figure 2b,e, respectively. EDX reveals a slight Sn excess on average through all the samples before curing. This excess can be explained by the surface sensitive technique XPS, which reveals a significant Sn enrichment (≈2:1) in the top 10 nm of the film. Whilst some of this excess observed is likely due to a preferential Se loss during the etching process conducted before XPS, as evident from the slight Sn oxidation seen in the peak humps seen in Figure 2c (for fitting see Figure S3, Supporting Information). This surface Sn enrichment is also believed to account for the lack of 1:1 stoichiometry observed on average through the bulk of the samples by EDX. The Sn surface enrichment can be explained by evaporation of Se whilst the inks are drying. This is believed to occur due a small amount of SeO_2 potentially being formed in the ink, which is soluble in water and could in part evaporate with water from the surface in the drying process.[36] In contrast no potential Sn side product is known to be soluble.[37] Postcuring at 873 K in He, whilst compositions remain mostly consistent, there is seen to be a slight further loss of Se. Due to the curing temperature being near the Se boiling point of 958 K, whilst significantly lower than the boiling point of Sn at 2876 K, this further loss of Se is believed to be due to preferential evaporation of unreacted Se over Sn. No discernible difference was observed in the work function from all binder concentrations studied, both before and after cure which can be observed in Figure 2f. A mean kinetic energy value for work function was measured at 4.05 eV, this is in line with previously reported density functional theory calculations for the work function of SnSe monolayers.[38]

2.2. Evaluation of Thermoelectric Properties

For thermoelectric characterization SnSe legs were fabricated as described in the experimental section using the pseudo-3D printing method depicted in Figure S4a–f in the Supporting Information. These were then cured, and a typical postcure sample was shown in Figure S4g in the Supporting Information. **Figure 3**a shows that all SnSe samples exhibit a similar trend in electrical conductivity compared to single crystal SnSe,[11] where a sharp increase in electrical conductivity is seen from circa 600 K leading to a maximum at around 800 K. Most binder percentages result in electrical conductivities similar to the *a*-axis at best; however, 4% binder is shown to exhibit the optimum compromise between enough binder to hold the SnSe particles together to lessen contact resistance, whilst containing minimal infiltration in the samples of nonconductive bridges between SnSe particles.[39] 4% binder exhibits a peak electrical conductivity of 33 S cm^{-1}. This peak in electrical conductivity is substantially higher than the ≈10.5 S cm^{-1} seen for the *a*-axis of single crystal SnSe, however, still lower than the ≈100 S cm^{-1} seen in the higher conductivity *b*-axis and *c*-axis in single crystal SnSe.[11] This value is directly comparable to polycrystalline SnSe values presented in the literature produced by SPS,[15–22] as seen in Figure S5a in the Supporting Information. The Seebeck coefficients seen in Figure 3b for the pseudo-3D printed samples all follow a similar trend as seen for single crystal SnSe, with a steadily increasing Seebeck coefficient up to ≈600 K, followed by a sharp drop up to 800 K after which the values appear stable. These trends in electrical conductivity and Seebeck coefficient are consistent with electronic band structure calculations of the decrease in bandgap (0.61–0.39 eV) between the lower temperature *Pnma* phase and the higher temperature *Cmcm* phase.[11] The lowest Seebeck values recorded were observed when using 4% binder; however, the values are still in line with, and in most cases in excess of, other SnSe manufacturing techniques in the literature, as shown in Figure S5b in the Supporting Information. Despite having the lowest Seebeck coefficient, due the higher electrical conductivity of the 4% binder ink, the power factor as seen in Figure 3c is shown to be the highest for this binder percentage. A maximum value of 280 μW m^{-1} K^{-2} is observed at 855 K. This is higher than the 212 μW m^{-1} K^{-2} seen for the *a*-axis of single crystal SnSe at 873 K,[11] but lower than the 765 μW m^{-1} K^{-2} at 873 K and 1003 μW m^{-1} K^{-2} at 823 K measured for the *c*-axis and *b*-axis in single crystal SnSe respectively. Figure S5c in the Supporting Information reveals that printed SnSe samples exhibit directly comparable power factors to SnSe manufactured in more energy and time intensive techniques.

The thermal conductivity of the printed samples, as shown in Figure 3d, were determined from the product of the thermal diffusivity (Figure S6a, Supporting Information), density (Figure S6b, Supporting Information), and heat capacity deduced from previous research ($\kappa = D\rho C_p$).[11,40] The thermal conductivity values can be seen to be similar to the values observed in single crystal SnSe. On average the values measured are lower than those seen for single crystal SnSe and most polycrystalline SnSe reported in the literature (Figure S5d, Supporting Information). To explain the reduced thermal conductivity (κ) of printed samples, Figure 3e shows both κ_e and κ_l for 4% binder which were determined using $\kappa = \kappa_e + \kappa_l$, where κ_e and κ_l are the electronic element from the charge carriers and the lattice element from the phonons toward thermal conductivity respectively. Wiedemann–Franz law was used to determine κ_e ($\kappa_e = L \cdot T \cdot \sigma$, assuming $L = 1.5 \times 10^{-8}$ V^2 K^{-2}).[11] The values are compared to the *a*-axis of single crystal SnSe, which reveals that the reduction in thermal conductivity is purely due to a reduction in the lattice component. This reduction in the lattice component can be explained when considering the binder. Postcure the binder will have been degraded, leaving in its place a nanoporous network. This nanoporous network would consequently result in a simultaneous reduction of the specific heat capacity (C_V), sound velocity (v), and the minimum phonon mean free path (l_{min}), lowering κ_l due to the relationship $\kappa_l = (1/3) \cdot C_V \cdot v \cdot l_{min}$.[41] Interestingly, the thermal conductivity of this nanoporous network is directly comparable the thermal conductivity of polycrystalline SnSe with a nanoporous design already presented in the literature, as shown in Figure S5d in the Supporting Information.[17] Any further reductions in thermal conductivity can

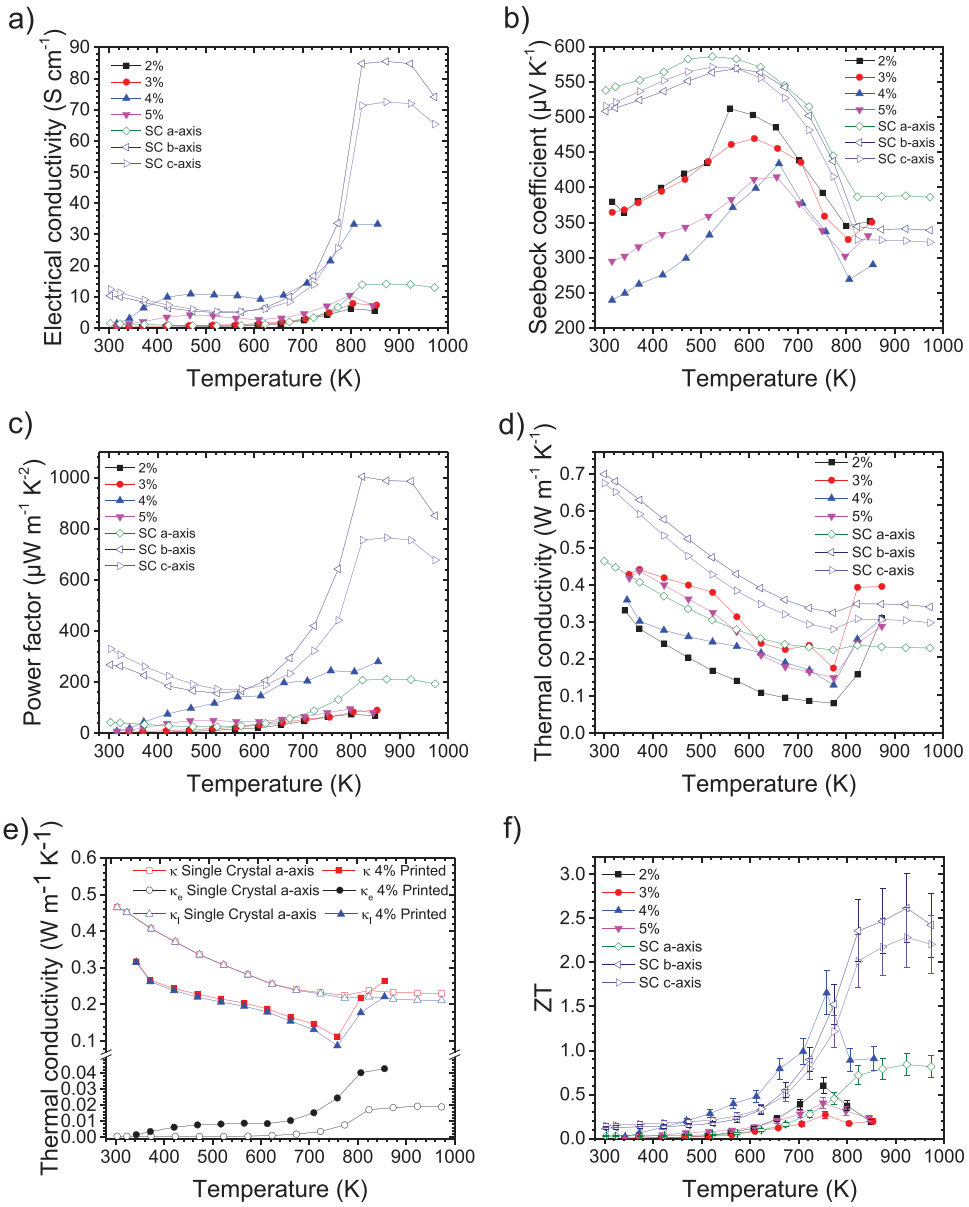

Figure 3. Thermoelectric performance of pseudo-3D printed SnSe with varying amounts of binder: a) electrical conductivity, b) Seebeck coefficient, c) power factor, d) thermal conductivity (κ), e) κ, κ_e, and κ_l of 4% binder compared to the *a-axis* of single crystal SnSe,[11] and f) figure of merit compared to single crystal SnSe,[11] with a measurement uncertainty of 15% represented with error bars.

be explained by thermal boundary resistances (Kapitza resistances) formed during the printing and annealing procedure. Figure 3f shows the highest ZT value of 1.7 (±0.25) at 758 K is observed when using 4% binder. This value exceeds the peak ZT of the *a*-axis of SnSe and at a lower temperature.

A comparison of the ZT value of 4% binder printed samples verses examples of polycrystalline SnSe in the literature is shown in **Figure 4**. The highest ZT value of 1.7 (±0.25) at 758 K is higher than many previously reported values of polycrystalline SnSe, which are mostly fabricated using high temperature and pressure techniques, such as SPS. The ZT profile of the cured printed nanoporous sample exhibits a similar ZT profile to previously reported polycrystalline nanoporous SnSe which exhibits a peak ZT of 1.7 (±0.2) at 823 K.[17] Significantly the peak ZT of 1.7 (±0.25) at 758 K is seen to be the highest known ZT to date for a printed thermoelectric material.

To test the stability and repeatability of the printed samples, the thermoelectric properties of samples containing 4% binder printed from separately synthesized inks were measured over three thermal cycles between room temperature and 873 K, and the results can be seen in Figure S7 in the Supporting Information. The results of the two samples from separately synthesized inks are very similar with ZT values mostly within error, indicating the high level of reproducibility of this work. The samples are seen to be very stable for both electrical conductivity and Seebeck coefficient and thus power factor. The thermal conductivity is seen to slowly rise on average with each temperature cycle. Due to the consistency in the electrical conductivity, Seebeck

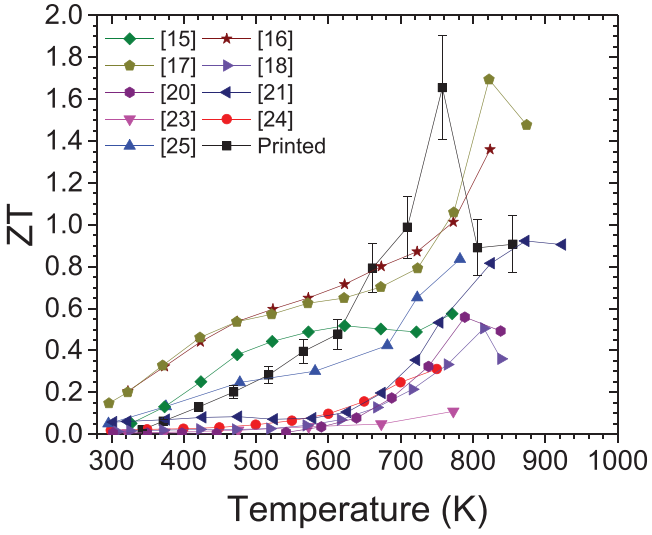

Figure 4. Figure of merit performance of pseudo-3D printed SnSe with 4% binder compared to polycrystalline SnSe reported in the literature, with a measurement uncertainty of 15% represented with error bars.

coefficient, and the minimal changes in grain sizes (as shown in Figure S8, Supporting Information), this rise in thermal conductivity is believed to be due to the gradual removal of the nanoporous network left behind from the degraded binder. The sharp increase in thermal conductivity from 758 K on the first measurement is thought to be the onset of the removal of nanoporosity because of a SnSe phase change from *Pnma* to *Cmcm* (≈807 K),[42] which results in the relatively low temperature peak ZT seen for the initial measurement when compared to single crystal and other polycrystalline SnSe examples in the literature. The increase in thermal conductivity leads to a gradual lowering of the average ZT on each measurement cycle; however, the ZT is still seen to exceed 1 on the 3rd cycle at 855 K. This importantly indicates that even without or with a significantly reduced nanoporosity, the samples still exhibit a relatively high ZT value for printed thermoelectric materials.

2.3. 3D Printed Thermoelectric Device Characterization

Using a 3D printed mask in which Cu tape was placed to allow a Z-type series connection when the elements are printed, a simple p-type thermoelectric generator was fabricated by infiltrating the mask with the SnSe ink. The ink and mask assembly were heated to 120 °C in air to allow the ink to be dried. After drying, the mask was cut away and aluminum heat sinks (14 mm × 14 mm × 7 mm) were attached to the top of each leg. The device fabrication technique and a device can be seen in **Figure 5**a–e and Figure 5f, respectively. The open-circuit voltage (V_0) and the short circuit current (I_0) can be seen in Figure 5h and the resulting power output of the device can be seen in Figure 5i (assuming maximum power = $V_0 I_0/4$[43]). The power of the device is shown to be significantly enhanced on cooling, compared to initially seen on heating. This is due to the device being uncured prior to testing. This increase in performance illustrates that the energy intensive curing step for these printed devices could be done in situ, thus keeping production costs of devices low. The peak output of the device

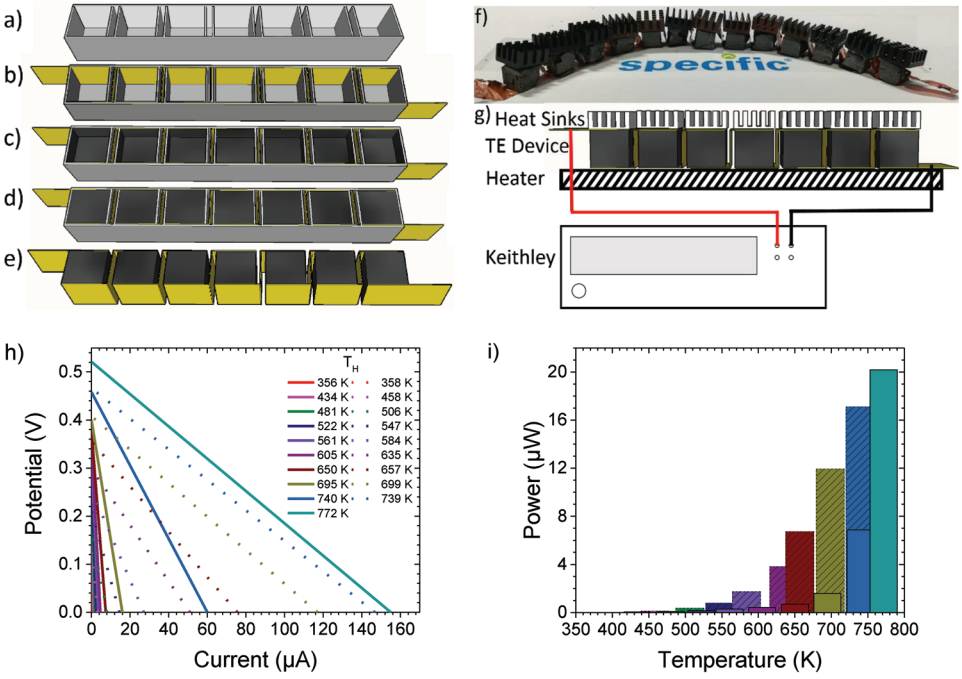

Figure 5. a–e) Fabrication of a printed SnSe thermoelectric device, f) photograph of a working device, g) schematic illustration of device performance setup, h) the open-circuit voltage (V_0) and the short-circuit current (I_0) linearly connected where solid lines represent values on heating whilst dotted lines represent values on cooling, i) peak power outputs of the device (assuming maximum power = $V_0 I_0/4$)[43] where solid bars represent power on heating whilst slashed bars represent power on cooling.

was 20 μW at 772 K. The power of the device is lower than the ZT values may suggest, this can be explained due to heat conduction through the device via the Cu tape, poor electrical contact between the tape and the SnSe legs, minimal passive cooling on the cold side of the device and the maximum hot temperature reached being significantly below the peak ZT of the SnSe inks and below the curing temperature previously used. Nonetheless the device is both the first reported multielement SnSe thermoelectric generator produced in standard leg geometry and the first printed non-Bi_2Te_3 thermoelectric generator produced from standard geometry elements which have been wholly printed. We believe this represents the first step to commercialization of the technology through further improvements, particularly through the development of an n-type leg in order to build a standard p-type and n-type leg pair.

3. Conclusions

P-type SnSe ink was produced with controllable grain sizes at low temperatures, an important step for printed SnSe thermoelectrics, photovoltaics, Li-ion and Na-ion batteries, and supercapacitors. Thermoelectric elements were successfully pseudo-3D printed using varying concentrations of the carboxymethylcellulose binder. The Seebeck coefficients of samples were seen to be comparable to the values seen in single crystal SnSe. Using 4% of the binder resulted in comparable electrical conductivities to those seen in single crystal. Significantly the electrical conductivity was higher than that seen in the single crystal *a*-axis and higher than even the more conductive single crystal *b* and *c* axes at lower temperatures. The thermal conductivity was seen to be on average lower than single crystal, and most polycrystalline SnSe in the literature. This is believed to be due to a nanoporous network left behind from degraded binder, and thermal boundary resistances from the printing and curing technique. A ZT of 1.7 (±0.25) was recorded at 758 K in 4% binder concentration, making this the highest known ZT of a printed thermoelectric material. A simple printed p-leg thermoelectric device was also printed, demonstrating the proof-of-concept of the printing technique whilst yielding the first printed SnSe thermoelectric device, which is the first medium to high temperature printed thermoelectric device. The challenge now is to manufacture elements that maintain their nanoporosity throughout thermal cycling, and to fabricate a printable n-type leg of comparable performance, to enable the manufacturing of efficient bulk thermoelectric generators.

4. Experimental Section

Ink Formulation: Sn (≥99%, Sigma-Aldrich) and Se (≥99.5%, Sigma-Aldrich) powders were added in equimolar quantities to a 250 mL stainless steel grinding bowl (Fritsch), to which stainless steel ball bearings (30) each of 10 mm in diameter were added. This was secured into a planetary mill (PULVERISETTE 5/2) and a sand filled grinding bowl was added as a counter balance. This was set to spin (200 rpm for 30 min) followed by a resting period of 30 min, this cycle was repeated 60 times. Binder solutions were made by mixing sodium carboxymethylcellulose (average $M_W \approx 250\,000$, Sigma-Aldrich) with deionized water in weight ratios to make 1%, 2%, 3%, 4%, and 5% by weight mixtures of carboxymethylcellulose in water. The binder mixing process was accelerated with the use of a centrifugal mixer (SpeedMixer DAC 150.1 FVZ).

Binder solution (13 g) was mixed with ball milled powder (37 g) in a centrifugal mixer (1500 rpm for 60 s), the mixture was then briefly agitated on a vortex genie and stirred with a spatula. This process was repeated until a uniform paste was produced.

Films were produced by spreading the paste on glass between two lines of Kapton tape 16 layers thick, which were then dried on a hot plate (120 °C for 10 min). The glass was then split down premade score lines to produces samples that were 22 mm × 10 mm. Samples were cured by heating to 873 K from room temperature at 0.5 K per minute, before being left to cool back to room temperature naturally.

Material Characterization: XRD was performed on a Brucker D8 diffractor with Cu K_α radiation. SEM and EDX were performed on a Joel 7800F field emission gun (FEG) SEM with an Oxford Laboratory EDX attachment.

XPS and ultraviolet photoelectron spectroscopy (UPS) were performed on a Kratos Axis Supra instrument and data were processed in CasaXPS (2.3.17dev6.4k). Samples were mounted in electrical contact with the stage to enable a 9 V sample bias during UPS and the Fermi edge of a clean Ag control was used to calibrate the energy scale to 0 eV. XPS sampled to a depth of <10 nm using a monochromatic K_α source (225 W, 15 mA) with a footprint 300 × 700 μm and a pass energy of 20 eV, with the GL(30) lineshape. For UPS the kinetic energy values of the secondary electron cutoff and valence band maximum were determined by fitting tangents (see Figure S9, Supporting Information) using the "step up" and "step down" regions from a He(I) (21.21 eV) photoemission spectrum with a 10 eV pass energy. The tangent fitting error specified by the manufacturer is ±0.13 eV.

Pseudo 3D Printing Technique: Legs of SnSe were created by using a sacrificial 3D printed acrylonitrile butadiene styrene (ABS) mask. Ink was poured into this at ≈2 mm thickness at a time, allowed to set at 120 °C on a hot plate for 10 min, before ≈2 mm more was added. This was repeated until a leg size of ≈1 cm was created. The technique is depicted in Figure S4 in the Supporting Information. These legs were then cured by heating to 873 K from room temperature at a heating rate of 0.5 K per minute, before being left to cool back to room temperature naturally.

Thermoelectric Characterization: Electrical and Seebeck coefficient measurements were conducted using an ULVAC ZEM-3 thermoelectric tester, in a He atmosphere. Sample dimensions were measured both before and after measurements, with no change in dimensions observed. Thermal diffusivities (D) were determined using a Netzsch 457 LFA with a Netzsch sapphire sample pan and lid for liquid metallic and powder samples, Ø 11 mm × 1.5 mm, and using the Cowon + pulse correction diffusivity model. This was calibrated with a 10 mm Ø Pyroceram 9606 calibration standard. Results are reported in Figure S6a in the Supporting Information. Heat capacities (C_p) were deduced from previous research.[11,40] Densities were determined using the method of hydrostatic weighing, that uses the Archimedes principle, with results reported in Figure S6b in the Supporting Information.[44]

Supporting Information

Supporting Information is available from the Wiley Online Library or from the author.

Acknowledgements

The authors wish to thank Engineering and Physical Sciences Council (EPRSC) (EP/N020863/1) for funding. N.P.L. and S.M. wish to thank the Welsh Government, European Regional Development Fund (ERDF) and SMARTExpertise Wales for funding Materials Advanced Characterisation Centre (MACH1) and Combinatorial Metallurgy (COMET). M.J.C. would like to thank ERDF and Welsh European Funding Office (WEFO) for funding of Solar Photovoltaic Academic Research Consortium (SPARC) II. All authors acknowledge the Swansea University Advanced Imaging in Materials (SU AIM) Facility (EPSRC EP/M028267/1) for microscopy and imaging. The authors would also like to thank Eric Don (Semimetrics

Ltd.) and Vincent Linseis (Linseis GmbH) for detailed discussions on this work. All data created during this research are openly available from the Swansea University data archive at https://doi.org/10.5281/zenodo.2163506. The authors would like to thank COATED2 (EPSRC EP/L015099/1) for purchasing the ULVAC ZEM-3.

Conflict of Interest

The authors declare no conflict of interest.

Keywords

3D, device, printing, thermoelectrics, tin selenide

Received: January 18, 2019
Revised: April 17, 2019
Published online:

[1] A. F. Joffe, L. S. Stil'bans, *Rep. Prog. Phys.* **1959**, *22*, 167.
[2] G. J. Snyder, E. S. Toberer, *Nat. Mater.* **2008**, *7*, 105.
[3] M. Zebarjadi, K. Esfarjani, M. S. Dresselhaus, Z. F. Ren, G. Chen, *Energy Environ. Sci.* **2012**, *5*, 5147.
[4] *CRC Handbook of Chemistry and Physics* (Ed: D. R. Lide), CRC Press, Boca Raton, FL **2005**.
[5] J. Yang, T. Caillat, *MRS Bull.* **2006**, *31*, 224.
[6] M. Kishi, H. Nemoto, T. Hamao, M. Yamamoto, S. Sudou, M. Mandai, S. Yamamoto, in *Eighteenth Int. Conf. Thermoelectr. Proc., ICT'99 (Cat. No. 99TH8407)*, IEEE, **n.d.**, Piscataway, NJ, USA **1999**, pp. 301–307.
[7] D. M. Rowe, *Thermoelectrics Handbook*, CRC Press, Boca Raton, FL, USA **2005**.
[8] J. W. Fergus, *J. Eur. Ceram. Soc.* **2012**, *32*, 525.
[9] A. Nozariasbmarz, A. Agarwal, Z. A. Coutant, M. J. Hall, J. Liu, R. Liu, A. Malhotra, P. Norouzzadeh, M. C. Öztürk, V. P. Ramesh, Y. Sargolzaeiaval, F. Suarez, D. Vashaee, *Jpn. J. Appl. Phys.* **2017**, *56*, 05DA04.
[10] T. Zhu, C. Fu, H. Xie, Y. Liu, X. Zhao, *Adv. Energy Mater.* **2015**, *5*, 1500588.
[11] L.-D. Zhao, S.-H. Lo, Y. Zhang, H. Sun, G. Tan, C. Uher, C. Wolverton, V. P. Dravid, M. G. Kanatzidis, *Nature* **2014**, *508*, 373.
[12] V. R. Minnam Reddy, S. Gedi, B. Pejjai, C. Park, *J. Mater. Sci.: Mater. Electron.* **2016**, *27*, 5491.
[13] Z. Wei, L. Wang, M. Zhuo, W. Ni, H. Wang, J. Ma, *J. Mater. Chem. A* **2018**, *6*, 12185.
[14] W. Shi, M. Gao, J. Wei, J. Gao, C. Fan, E. Ashalley, H. Li, Z. Wang, *Adv. Sci.* **2018**, *5*, 1700602.
[15] Y. Li, F. Li, J. Dong, Z. Ge, F. Kang, J. He, H. Du, B. Li, J.-F. Li, *J. Mater. Chem. C* **2016**, *4*, 2047.
[16] X. Shi, Z.-G. Chen, W. Liu, L. Yang, M. Hong, R. Moshwan, L. Huang, J. Zou, *Energy Storage Mater.* **2018**, *10*, 130.
[17] X. Shi, A. Wu, W. Liu, R. Moshwan, Y. Wang, Z.-G. Chen, J. Zou, *ACS Nano* **2018**, *12*, 11417.
[18] S. Sassi, C. Candolfi, J.-B. Vaney, V. Ohorodniichuk, P. Masschelein, A. Dauscher, B. Lenoir, *Appl. Phys. Lett.* **2014**, *104*, 212105.
[19] T.-R. Wei, G. Tan, X. Zhang, C.-F. Wu, J.-F. Li, V. P. Dravid, G. J. Snyder, M. G. Kanatzidis, *J. Am. Chem. Soc.* **2016**, *138*, 8875.
[20] Y. Li, X. Shi, D. Ren, J. Chen, L. Chen, *Energies* **2015**, *8*, 6275.
[21] Y. Fu, J. Xu, G.-Q. Liu, J. Yang, X. Tan, Z. Liu, H. Qin, H. Shao, H. Jiang, B. Liang, J. Jiang, *J. Mater. Chem. C* **2016**, *4*, 1201.
[22] Y. Gong, C. Chang, W. Wei, J. Liu, W. Xiong, S. Chai, D. Li, J. Zhang, G. Tang, *Scr. Mater.* **2018**, *147*, 74.
[23] J. O. Morales Ferreiro, D. E. Diaz-Droguett, D. Celentano, J. S. Reparaz, C. M. Sotomayor Torres, S. Ganguli, T. Luo, *Appl. Therm. Eng.* **2017**, *111*, 1426.
[24] C.-L. Chen, H. Wang, Y.-Y. Chen, T. Day, G. J. Snyder, *J. Mater. Chem. A* **2014**, *2*, 11171.
[25] E. K. Chere, Q. Zhang, K. Dahal, F. Cao, J. Mao, Z. Ren, *J. Mater. Chem. A* **2016**, *4*, 1848.
[26] M. R. Burton, T. Liu, J. McGettrick, S. Mehraban, J. Baker, A. Pockett, T. Watson, O. Fenwick, M. J. Carnie, *Adv. Mater.* **2018**, *30*, 1801357.
[27] G. Jeong, Y. H. Jaung, J. Kim, J. Y. Song, B. Shin, *J. Mater. Chem. C* **2018**, *6*, 10083.
[28] S. Shin, R. Kumar, J. W. Roh, D.-S. Ko, H.-S. Kim, S. Il Kim, L. Yin, S. M. Schlossberg, S. Cui, J.-M. You, S. Kwon, J. Zheng, J. Wang, R. Chen, *Sci. Rep.* **2017**, *7*, 7317.
[29] Z. Cao, M. J. Tudor, R. N. Torah, S. P. Beeby, *IEEE Trans. Electron Devices* **2016**, *63*, 4024.
[30] F. Kim, B. Kwon, Y. Eom, J. E. Lee, S. Park, S. Jo, S. H. Park, B.-S. Kim, H. J. Im, M. H. Lee, T. S. Min, K. T. Kim, H. G. Chae, W. P. King, J. S. Son, *Nat. Energy* **2018**, *3*, 301.
[31] C. Han, G. Tan, T. Varghese, M. G. Kanatzidis, Y. Zhang, *ACS Energy Lett.* **2018**, *3*, 818.
[32] A. T. Duong, V. Q. Nguyen, G. Duvjir, V. T. Duong, S. Kwon, J. Y. Song, J. K. Lee, J. E. Lee, S. Park, T. Min, J. Lee, J. Kim, S. Cho, *Nat. Commun.* **2016**, *7*, 13713.
[33] C. H. Suen, D. Shi, Y. Su, Z. Zhang, C. H. Chan, X. Tang, Y. Li, K. H. Lam, X. Chen, B. L. Huang, X. Y. Zhou, J.-Y. Dai, *J. Mater.* **2017**, *3*, 293.
[34] H. Do Kim, H. Ohkita, H. Benten, S. Ito, *Adv. Mater.* **2016**, *28*, 917.
[35] M. Takashiri, K. Miyazaki, S. Tanaka, J. Kurosaki, D. Nagai, H. Tsukamoto, *J. Appl. Phys.* **2008**, *104*, 084302.
[36] R. S. Carmichael, *Practical Handbook of Physical Properties of Rocks and Minerals (1988)*, CRC Press, Boca Raton, FL, USA **2017**.
[37] W. M. Haynes, *CRC Handbook of Chemistry and Physics, 95th Edition*, CRC Press, Boca Raton, FL, USA **2014**.
[38] Z. Cui, X. Wang, Y. Ding, M. Li, *Superlattices Microstruct.* **2018**, *114*, 251.
[39] R. Strümpler, J. Glatz-Reichenbach, *J. Electroceram.* **1999**, *3*, 329.
[40] L.-D. Zhao, G. Tan, S. Hao, J. He, Y. Pei, H. Chi, H. Wang, S. Gong, H. Xu, V. P. Dravid, C. Uher, G. J. Snyder, C. Wolverton, M. G. Kanatzidis, *Science* **2016**, *351*, 141.
[41] K. Zhao, H. Duan, N. Raghavendra, P. Qiu, Y. Zeng, W. Zhang, J. Yang, X. Shi, L. Chen, *Adv. Mater.* **2017**, *29*, 1701148.
[42] H. Wiedemeier, F. J. Csillag, *Z. Kristallogr. - Cryst. Mater.* **1979**, *149*, 17.
[43] P. Fan, Z. Zheng, Y. Li, Q. Lin, J. Luo, G. Liang, X. Cai, D. Zhang, F. Ye, *Appl. Phys. Lett.* **2015**, *106*, 073901.
[44] A. Smakula, V. Sils, *Phys. Rev.* **1955**, *99*, 1744.